



Uniaxial compaction of sand using 4D X-ray tomography: The effect of mineralogy on grain-scale compaction mechanisms

Andrea Cuesta Cano, Jeroen F. Van Stappen^{1,*}, Timotheus K.T. Wolterbeek, Suzanne J.T. Hangx

High Pressure and Temperature Laboratory, Department of Earth Sciences, Faculty of Geosciences, Utrecht University, Utrecht, the Netherlands

ARTICLE INFO

Keywords:

Sand pack compaction
Mineralogy effect
Micro X-ray computed tomography
Quartz
Potassium feldspar
Clays
Inelastic deformation processes

ABSTRACT

The mechanical behaviour of sand aggregates is often studied as a proxy for poorly consolidated sands and highly porous sandstones. Only recently research aimed at understanding sand deformation has started to use techniques that allow for direct observation of the in-situ grain-scale processes. Using state-of-the-art, time-lapse micro X-ray computed tomography (micro-XCT) imaging, the influence of mineralogy on the compaction of sand aggregates has been investigated by performing uniaxial compaction experiments on four different mineral assemblages (quartz, K-feldspar, quartz + K-feldspar and quartz + K-feldspar + clay) at room temperature and dry conditions. For the experiments, a bespoke uniaxial compaction device (sample diameter 2 mm) was constructed and coupled with micro-XCT imaging. This enabled in-situ observation of the strain-accommodating processes during deformation. To verify that the microstructural evolution observed in the small-scale experiments is representative for larger aggregate behaviour, conventional, centimetre-sized, control experiments were performed. The observed inelastic deformation was mainly accommodated by processes such as intragranular cracking and intergranular sliding. At low axial stresses (10 MPa), grain fracturing mainly occurred in K-feldspar grains, if present, along cleavage planes. Only at higher axial stresses, fracturing of quartz grains, if present, was also observed. Presence of clays, in pores and grain contacts, delayed the onset of quartz grain breakage and enhanced porosity reduction as clay in grain contacts facilitated grain sliding and rearrangement.

1. Introduction

Globally, many hydrocarbon reservoirs consist of highly porous, unconsolidated sands [1] or poorly consolidated sandstones [2]. Prolonged hydrocarbon production often leads to compaction of these reservoirs, which can be expressed at the surface as subsidence [3,4]. In fractured reservoirs, differential compaction across faults can also result in induced seismicity [5,6]. Reservoir compaction is caused by pore pressure reduction, resulting from fluid extraction, and a concomitant increase in the effective overburden stress [3]. Studies have shown that compaction at the reservoir level is not fully recoverable (i.e. poro-elastic), but can also involve significant permanent (i.e. inelastic) deformation [2,7,8]. The latter is caused by grain-scale processes, such as intergranular and intragranular fracturing, mass transfer processes, and/or frictional sliding along grain contacts, potentially aided by the deformation of thin intergranular clay films [2,3,7,8]. Therefore, it is important to understand and quantify the grain-scale mechanisms leading to reservoir compaction.

To investigate these grain-scale mechanisms, loose sand aggregates have been extensively studied as analogues for poorly consolidated sands and sandstones [9–14], making use of first-order similarities in their mechanical behaviour. However, a key difference between sands and sandstones is the presence of a cementing phase [15,16]. Cementation, even when present in small quantities, typically increases the strength of granular materials, preventing stress concentration at grain-to-grain contacts and resulting in a more even stress distribution [17–19]. In sandstones, failure, sliding and rotation of grains are therefore less pronounced than in loose sands. Besides being a proxy for sandstone behaviour, the geomechanical response of compacting reservoir sands is also directly relevant to sediment compaction prior to diagenesis. This is applicable to basins with a low geothermal gradient and fast burial rate, where high overburden stresses can be reached before quartz cementation occurs [20,21].

An extensive body of work exists on the compaction behaviour of sands, focusing on assessing the influence of factors like initial porosity, grain angularity, grain shape, grain size (distribution), intrinsic grain

* Corresponding author.

E-mail address: j.f.vanstappen@uu.nl (J.F. Van Stappen).

¹ Currently at: PProGress – UGCT, Department of Geology, Faculty of Sciences, Ghent University, Ghent, Belgium.

strength, type of grain contacts, and chemical environment [9,10,12,20–25]. From these studies, it is known that sand compaction increases with increasing initial aggregate porosity, increasing grain angularity, size and size uniformity, decreasing intrinsic strength and the presence of aqueous fluids. By contrast, relatively few studies have focused on the influence of mineralogy on sand compaction [20,21,23]. Yet, in nature, rocks rarely consist of monomineralic assemblies.

To date, the grain-scale mechanisms leading to inelastic deformation are typically assessed through laboratory experiments performed under representative, in-situ conditions, with microstructural analysis of 2D thin sections of post-experiment (deformed) and reference samples using optical [9,26] or scanning electron microscopy (SEM) [2]. Through the localization of acoustic emission (AE) events during deformation, a 3D image of locations of grain sliding or failure can be created under in-situ stress conditions [10,27,28]. However, in practice this technique relies on the generation of audible acoustic emissions, limiting AE monitoring to grain-scale mechanisms that release sufficient energy during deformation, while mechanisms such as intergranular clay compaction [29] may not lead to audible AEs. At the same time, it does not allow for visual confirmation of the actual deformation mechanism causing the acoustic event, meaning post-experimental microstructural analysis is still necessary [10]. With the development of time-lapse micro X-ray computed tomography (4D micro-XCT), it is now possible to perform experiments to investigate the real-time evolution of the internal structure of materials during deformation [12,30]. Recent studies employed micro-XCT techniques to study the effect of grain shape and coordination number on mechanical behaviour [31–34], the evolution of particle breakage [35,36] and deformation localisation [37,38]. Some studies also focused on the image processing issues of resolving fines and characterising the contacts between particles [39].

In this contribution, the impact of mineralogy on the inelastic processes related to time-independent sand compaction is systematically analysed. To this end, 4D micro-XCT, uniaxial compaction experiments have been performed on simulated reservoir sand aggregates (sample diameter 2 mm) under dry conditions and at room temperature. The results have been compared to control experiments performed in a conventional oedometer (sample diameter 19.4 mm) to assess the effect of sample size on microstructural evolution. Tested aggregates consist of pure quartz and pure feldspar sand, as well as quartz-feldspar and quartz-feldspar-clay mixtures. These mineral assemblies cover the range from relatively clean sands observed in deep water turbidite systems, such as in the Gulf of Mexico [40,41], to polymineralic sand mixtures, representing the mixed fluvial-aeolian depositional settings of desert environments, such as seen in the Groningen Gas Field, The Netherlands [42,43].

2. Materials and methods

2.1. Sample preparation

2.1.1. Starting materials

Quartz (Qz) sand was obtained from the Heksenberg Member of the Breda Formation [44], at the Beaujean quarry near Heerlen, The Netherlands [9]. The quartz content is >99 wt%, with zircon and Na-rich feldspar as the main trace minerals and minor presence of iron oxide/hydroxide coatings. SEM-imaging shows that the sand grains are subrounded and have a generally smooth surface [9]. The Qz sand was sieved to a grain size fraction of $196 \pm 16 \mu\text{m}$. Potassium feldspar (Kfs) sand was commercially obtained from Amberger Kaolinwerke as Feldspar FS 900 S. It consists of 87% K-feldspar and 7% Na-feldspar, with minor traces of clays and quartz. As for the Qz sand, the Kfs sand was sieved to obtain a grain size fraction of $196 \pm 16 \mu\text{m}$. The clay material (C) used for this study was obtained from The Clay Minerals Society as SAz-1, which is a Ca-montmorillonite from the Bidahochi Formation (Pliocene) in Arizona, USA. It is a high charge ($\text{CEC} = 120 \text{ cmolc kg}^{-1}$) Arizona clay type, with Ca^{2+} and K^{+} as the main interlayer cations and

minor amounts of Na^{+} [45].

2.1.2. Barium-substitution in clay: enhancing attenuation contrast

Tests have shown that the Arizona clay displays X-ray attenuation similar to the Qz and Kfs grains, resulting in limited to no contrast in grey-values in the micro-XCT images. To enhance contrast, the clay was chemically altered through a cation exchange reaction [46], by substituting the Ca^{2+} interlayer cations with Ba^{2+} , to increase clay attenuation [19]. This Ca/Ba-cation exchange reaction was selected, based on theoretical attenuation patterns predicted using scanner simulator Arion, specifically built to replicate X-ray CT scans on the systems available at the Centre for X-ray Tomography at Ghent University (UGCT) [47,48]. The procedure of using this scanner simulator is explained in Appendix A. Based on theoretical graphs for the linear attenuation of quartz, untreated Arizona clay, and Ba^{2+} -substituted Arizona clay, there is a significant difference in X-ray attenuation for the untreated and Ba^{2+} -substituted Arizona clays at relevant X-ray photon energies (Fig. A1c).

For the cation exchange, 8.48 g of SAz-1 was reacted with 100 ml of 0.1 M BaCl_2 solution for 14 days. During this period, the barium chloride solution was replaced seven times, i.e. roughly every two days, to maximize the exchange potential. After 14 days, the solution was decanted off the clay residue. To prevent the formation of salt crystals, the residue was subsequently washed four times by adding a 50–50 volume mixture of distilled water and ethanol, and stirring for 3 min. After decanting off the excess fluid and washing, the ion-exchanged clays were oven-dried for 5 days at 50°C . The clays were subsequently crushed and sieved to obtain a particle size fraction of less than $63 \mu\text{m}$, to reflect typical clay grain sizes observed in intergranular clay layers and pore-filling clays in sandstones [49–51].

2.2. Experimental set-up and procedures

All experiments were performed at room temperature and under lab-dry conditions, to avoid any fluid-enhanced time-dependent compaction behaviour during scanning. Four micro-XCT experiments (2 mm diameter) were performed, complemented by five conventional uniaxial compaction experiments on pure Qz sand samples, performed using an oedometer-type setup (vessel internal diameter 19.4 mm).

2.2.1. Uniaxial compaction apparatus for micro-XCT experiments

A bespoke, small-scale uniaxial compaction cell was built to fit on top of a Deben CT5000 in-situ testing stage, already available at the UGCT. The Deben CT5000 apparatus is conventionally used to perform unconfined tensile or compressive tests on samples with diameters of 10–20 mm [52], by applying an axial force of up to 5 kN. The new uniaxial compaction vessel has an inner diameter of 2 mm, which is equivalent to the sample diameter, allowing us to use loose sand aggregates and attain a higher spatial resolution during micro-XCT imaging, required to visualize the grain-scale compaction mechanisms. Note this diameter exceeds ten times the chosen grain size fraction, which is the minimum ratio required for reproducibility in geomechanical experiments on well-sorted granular materials [53–55]. The uniaxial compaction apparatus, or MARISCA device (Miniature Axial Rig for In-situ Scanning of Compressed Assemblies), is shown in Fig. 1. The sand sample is contained within a polyether-ether-ketone (PEEK) container (Fig. 1c). PEEK spacers are placed at the top and bottom of the aggregate. The assembly is covered by a PEEK endcap, which prevents upward movement of the assembly, and is screwed onto the aluminium base of the MARISCA device. Compaction of the sand aggregate is achieved by displacement of a lower, stainless steel driving piston, located in the assembly base (Fig. 1a), which is driven up by the motor inside the Deben CT5000 testing stage at a constant displacement rate of 0.1 mm min^{-1} . Given the strength of PEEK, axial forces of up to 220 N can be achieved with the current set-up, allowing axial stresses of up to 70 MPa to be applied on the 2 mm-diameter samples.

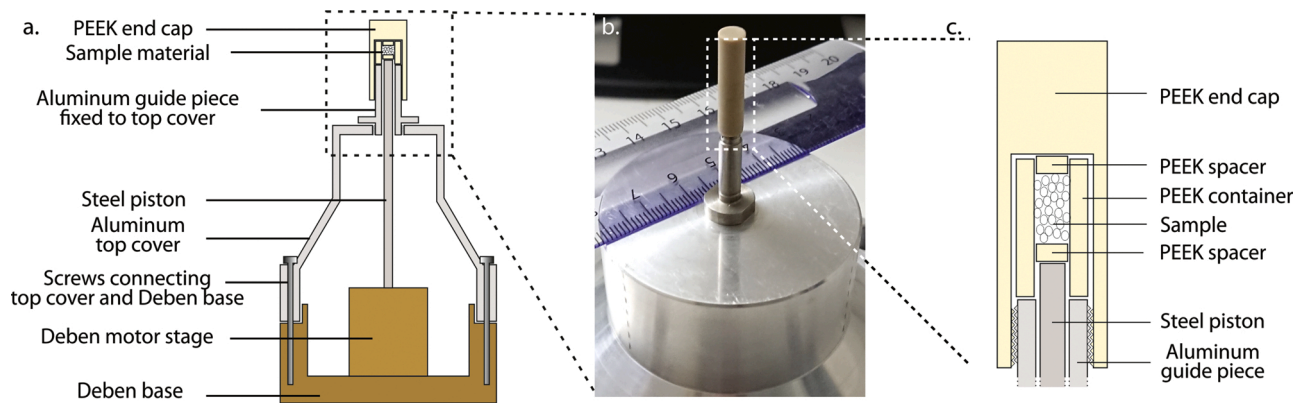


Fig. 1. a) Overview of the MARISCA uniaxial compaction device. b) Photograph of the upper part of the MARISCA device, showing the PEEK end cap, screwed on an aluminium guide piece, fitted on the top cover of the Deben base. c) Details of the sample vessel showing the PEEK container holding the sand aggregate, confined between two PEEK spacers. The steel bottom piston drives deformation, while the PEEK endcap ensures that the container holding the sample remains stationary.

2.2.2. Experimental procedure and time-lapse micro-computed tomography imaging

Prior to each test, a PEEK spacer was placed at the bottom of the PEEK sample container, on top of the steel bottom piston, followed by a 5 μm thick, polytetrafluoroethylene (PTFE, Teflon) liner along the container walls. Since some grains may be pressed into the PEEK spacers during compaction, these were replaced upon each subsequent test. The Teflon liner minimized friction between the sand aggregate and PEEK vessel, by preventing grain embedment, and thus reduced end-effects within the sample. Tests were performed on sand samples with initial lengths varying between 1.4 and 2.4 mm. For the KfsQz sand mixture, about 3 g of stock material was prepared by combining and mixing K-feldspar and quartz sand in a 30:70 feldspar:quartz solid volume ratio. From this stock mixture, a small subsample of 5–10 mg was placed in the MARISCA device. However, due to the small sample size, the actual Kfs and Qz contents of the sample deviated slightly from the 30–70 vol % distribution in the stock mixture, despite careful mixing. Upon analysis of the sample during image processing, it was shown that the actual aggregate contained 20 vol.% Kfs and 80 vol.% Qz. Similarly, for the KfsQzC sand mixture, a stock mixture of 20 vol.% clay, 10 vol.% Kfs and 70 vol.% Qz was prepared. Despite the contrast-enhancing procedure applied to the clay, it was not possible to accurately determine the KfsQzC composition during the experiment (see Section 2.2.3 and Appendix B).

Each sample was carefully deposited in the PEEK container using a narrow, paper funnel, in order to prevent grains from sticking to the container wall, followed by gentle tapping of the vessel to ensure settling of the sample. The Qz, Kfs and KfsQz samples were emplaced dry, while the KfsQzC sample was premixed with ethanol, to improve homogenisation and to coat the Kfs and Qz grains with the clay material. After emplacement, the KfsQzC sample was allowed to dry prior to further use. Subsequently, the top spacer was inserted, followed by the PEEK endcap. The whole assembly was screwed onto the Deben CT5000 base until a force of 3.5 N was measured by the Microtest software, indicating that the top spacer and the end cap touched, and the bottom piston was able to exert force on the sample.

The MARISCA device was placed on the Environmental Micro-CT scanner (EMCT) [56,57]. This scanner employs a gantry-based system in which the X-ray source and detector rotate around the sample, thereby eliminating rotational issues regarding the electrical wires required to control the MARISCA device. The EMCT scanner is equipped with an XWT 240-SE microfocus X-ray source and an active pixel flat panel detector. In combination with the MARISCA device, an image resolution with a voxel size of 5.0 μm was obtained during the 4D deformation experiments. For each micro-XCT scan, 800 projections were taken over 360°, which took approximately five minutes. Each projection was constructed by the average of four radiographs, with a

single radiograph having an exposure time of 92 ms to increase image quality. All scans were performed at an acceleration voltage of 120 keV and 8 W output power. Using open beam and dark images, the projections were normalised and the Octopus software suite [58] was used to reconstruct the images.

At the start of each experiment, the bottom piston was driven upwards until an axial stress of 1.5 MPa (in the case of the Qz assembly) or 5 MPa (for the Kfs, KfsQz and KfsQzC assemblies) was reached, achieving a (nearly) locked aggregate. Subsequently, the loading piston was arrested, allowing the sample to relax. After one minute of sample relaxation, a micro-XCT scan was made. These initial scans at 1.5/5 MPa have been taken as the starting condition (time = 0) of the experiments. After taking the first scan, the axial stress on the sample was increased to 20 MPa for the Qz assembly and 10 MPa for the Kfs, KfsQz and KfsQzC assemblies, at a constant displacement rate of 0.1 mm min⁻¹, followed by another scan. Subsequently, the stress was progressively increased, in steps of 5 MPa, and micro-XCT scans were obtained for each step until a maximum axial stress of 50 MPa was reached. After the scan at 50 MPa, the sample was unloaded in a single step to the initial stress of 1.5/5 MPa, scanned, and then reloaded to 50 MPa in a single step, followed by a final micro-XCT scan. In total, ten scans were obtained for the Qz sand, while twelve scans were obtained for each of the Kfs, KfsQz and KfsQzC sands, resulting in a 4D representation of the compacting aggregates. All experiments were performed dry and at room temperature.

2.2.3. Image processing

For analysis of the micro-XCT images, two commercial software packages were used, namely: i) the open-source package Fiji [59] and ii) Avizo®, distributed by Thermo Fisher Scientific, Inc., [60]. Fiji has been used to obtain systematic measurements of the samples' length and diameter throughout the experiments. Avizo® offers an optimized workflow for material characterization in 2D and 3D. Using the Avizo® software, a “non-local means” filter was applied to remove noise from the CT-image data, followed by an interactive threshold, based on the different grey levels of each mineral, to obtain a quantification of the sample volume and pore volume within the vessel (see Appendix B). To separate individual grains in the thresholded images, the Avizo® watershed method was used. Due to differences in grey value between the quartz and feldspar grains, it was possible to determine the grain size distribution of the different components in the Qz, Kfs and KfsQz assemblies. Segmentation of the clay particles was hindered due to strong partial volume effects and consequently no grain size distribution analysis could be performed for the KfsQzC assembly. Detailed information on the segmentation and grey value overlap of the different minerals is provided in Appendix B.

Measurements of the sample length were used to obtain the axial strain, e (%), defined as $e = (\Delta L/L_0) \cdot 100\%$, where L_0 (mm) is the initial

length of the sample as obtained from the first scan and ΔL (mm) is the change in length due to compaction. Note that in these 1-D experiments, volumetric strain is equal to the axial strain. The total axial strain, $e_{\text{tot}}(\%)$, includes components of both elastic, $e_{\text{el}}(\%)$, and inelastic (permanent; $e_{\text{inel}}(\%)$) deformation, i.e. $e_{\text{total}} = e_{\text{el}} + e_{\text{inel}}$. The total inelastic strain can be determined from the unloading data (residual strain at 1.5/5 MPa).

The aggregate porosity, φ (-), is defined as $\varphi = 1 - V_s/V_t$, where V_s (mm^3) is the volume of the solid material (grains + Teflon liner) within the PEEK container and V_t (mm^3) is the total volume of the container. The total volume is calculated assuming that the sample can be approximated as a cylinder of length L_x (mm) and diameter D_x (mm), which are determined from independent measurements for each scan. The solid volume of the sample, V_s (mm^3), was calculated on the basis of the grey scale micro-XCT images, using Avizo®. Further details on the calculation of sample properties, including propagation of experimental errors, are provided in Appendix C. Initial porosity values of the small-scale experiments, obtained at the reference stresses, range from $39.4 \pm 1.0\%$ and $41.6 \pm 1.1\%$ for the pure Qz and Kfs samples, respectively, to $42.4 \pm 0.7\%$ for the KfsQz mixture and $32.9 \pm 0.9\%$ for the KfsQzC mixture.

2.2.4. Grain size analyses

For the grain size analyses of the MARISCA device experiments, the different minerals are thresholded and separated using a watershed segmentation [61]. Through this method, the 3D volume of each individual grain within the sample can be calculated using Avizo®. Though the grains are not spherical, the 3D grain volume data can be represented in terms of a so-called equivalent diameter, i.e. as an idealised sphere of equal volume. Due to image noise, individual grains composed of too few voxels are not considered in the grain size analysis. Therefore, a cut-off value of $10 \mu\text{m}$ was selected, as lower bound for the equivalent grain diameter included in the grain size distribution analysis.

2.3. Control experiments: centimetre-sized, conventional oedometer tests

To facilitate comparison with the mm-sized micro-XCT imaging experiments on quartz, in terms of the microstructural evolution of the samples, five oedometer-type compaction tests were performed on pure Qz sample material with the same grain size distribution ($196 \pm 16 \mu\text{m}$), aimed at retrieving the sand aggregate post-experiment. The five control experiments follow the same loading-unloading path as imposed on the Qz sample using the MARISCA device. Each control experiment was halted at different stages during the loading history, to preserve intermediate microstructures (i.e. grain size distributions). These control experiments were performed using a Remanit-4122 uniaxial compaction cell, located inside an Instron 8562 loading frame [62–64].

All five Qz control experiments were performed on individual sand samples ($9.13 \pm 0.18 \text{ g}$) under dry conditions at room temperature. At the start of each experiment, a Teflon liner was placed in the vessel and, then, the sand sample was carefully funnelled into the compaction vessel (inner diameter 19.4 mm). The initial sample length ($19.15\text{--}20.45 \text{ mm}$) was subsequently determined using the Instron LVDT as a measure of piston location. This procedure led to reasonably reproducible initial porosities of $38.8 \pm 1.1\%$. Note that the average porosity for these larger-scale quartz experiments is within the same range as for the small-scale quartz experiments ($39.4 \pm 1.0\%$). Individual experiments were performed up to maximum applied stresses of 20 MPa, 30 MPa, 40 MPa and 50 MPa, respectively, with the fifth experiment being loaded to 50 MPa, unloaded and reloaded to 50 MPa. After the pre-determined maximum applied stress was achieved, the sample was unloaded and carefully removed from the sample vessel. The grain size distributions of the retrieved quartz aggregates were determined using a Malvern Instruments Mastersizer S long bed particle sizer [65], i.e. on the basis of laser diffraction measurements. To facilitate comparison with the size distributions obtained from micro-XCT analysis, which was unable to

resolve grains $<10 \mu\text{m}$ in size (see Section 2.2.4), the Malvern particle sizer data was also cut off at a grain size of $10 \mu\text{m}$, removing fractions of very fine, pulverized material. Doing so omitted grains constituting $<1.5 \text{ vol}\%$ of the samples. A more detailed description of these methods is provided in Appendix D.

3. Results

A total of four micro-XCT, uniaxial compaction experiments has been performed using the MARISCA device. Note that the initial conditions are defined at 1.5 MPa for the Qz sample, while the initial state was defined at 5 MPa for the other samples (see Section 2.2.2). Key experimental results are summarized in Table 1, including data on the initial length (defined at 1.5/5 MPa), diameter and porosity of the samples, length at 50 MPa (before unloading), strain developed at 50 MPa (before the first unloading), and permanent strain (after the first unloading to 1.5/5 MPa).

3.1. Mechanical data

The applied axial stress versus axial strain data for all four MARISCA device experiments is displayed in Fig. 2a. All tests show similar behaviour, with a rapid increase in axial strain at low applied stresses up to 20 MPa, followed by a roughly linear increase in stress-strain behaviour up to the maximum axial stress, showing a continuous stiffening of the samples. It should be noted that over half of the total axial strain is accumulated during the initial 20 MPa axial stress. Likely this is caused in part by settling of the Teflon liner at low applied stresses (Fig. 4), as liner-free experiments (not included in this manuscript) did not show this slow initial ‘onramp’, though they suffered from grain embedment into the PEEK vessel. The total axial strain appears to be controlled by aggregate composition and initial porosity. The Qz aggregate displayed the lowest permanent strain, though its porosity was comparable to that of the Kfs and KfsQz samples. By contrast, the KfsQz and KfsQzC samples showed similar amounts of strain, though the latter had a 10% lower initial porosity.

As can be seen from the unloading data, the permanent strain is lowest for the pure Qz sample ($22.47 \pm 0.92\%$), followed by the KfsQzC ($25.92 \pm 0.84\%$) and KfsQz ($27.80 \pm 0.39\%$) aggregates. The largest permanent strain is observed for the pure Kfs sample ($34.38 \pm 1.17\%$). Upon reloading, 1.96–2.46% additional (apparent) strain is measured for samples Kfs, KfsQz and KfsQzC and 3.26% for sample Qz, which is slightly more than the elastic strain predicted from the total and

Table 1

Uniaxial compaction experiments performed on dry sand aggregates using the MARISCA device at room temperature. Initial dimensions and porosity were determined at an applied reference stress of 5 MPa, except for sample Qz for which the reference stress was 1.5 MPa. These same stress conditions were employed to determine the permanent strain after unloading to the reference stress. Errors are included for all the measurements (see Appendix C).

Sample	Initial length (mm)	Initial diameter (mm)	Initial porosity (%)	Length at 50 MPa (mm)	Strain at 50 MPa (%)	Permanent strain (%)
Qz	2.425 ± 0.009	1.962 ± 0.009	39.4 ± 1.0	1.827 ± 0.013	24.68 ± 0.20	22.47 ± 0.25
Kfs	1.759 ± 0.011	1.965 ± 0.007	41.6 ± 1.1	1.134 ± 0.013	35.51 ± 0.46	34.38 ± 0.55
KfsQz	1.926 ± 0.006	1.967 ± 0.007	42.4 ± 0.7	1.369 ± 0.008	28.91 ± 0.19	27.80 ± 0.12
KfsQzC	1.426 ± 0.010	1.972 ± 0.006	32.9 ± 0.9	1.056 ± 0.008	27.66 ± 0.30	25.92 ± 0.22

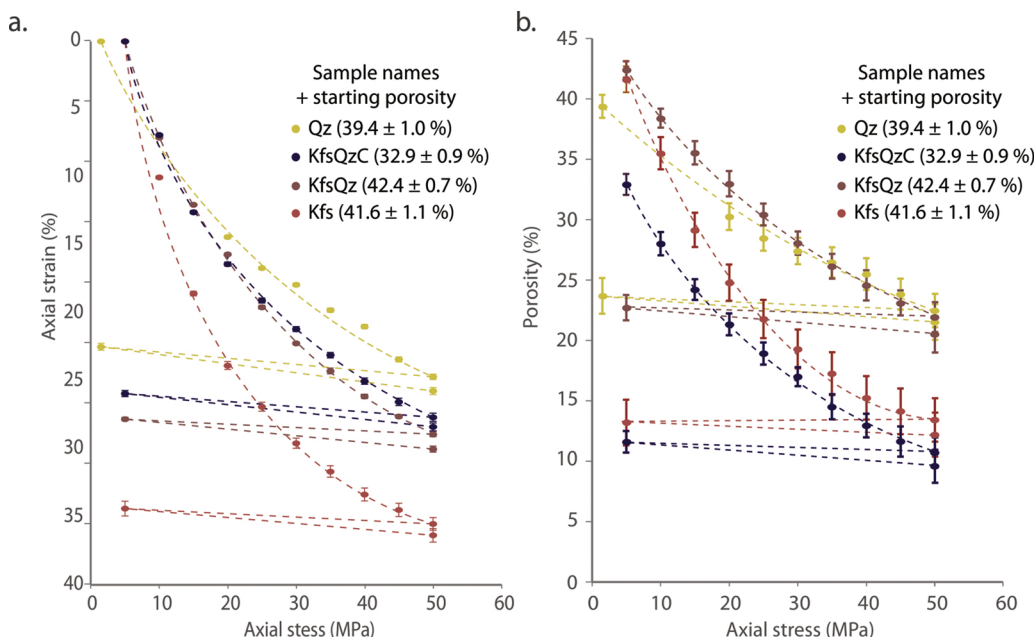


Fig. 2. a) Axial strain (%) and b) porosity (%) versus axial stress (MPa) for the micro-XCT uniaxial compaction experiments on dry sand aggregates at room temperature (Qz = quartz, Kfs = K-feldspar, C = montmorillonite clay). Fits through the data, intended to guide the eye, are shown by dashed lines. Strain is based on sample length change as measured from the micro-CT images. Porosity is based on vessel volume change and the solid volume obtained using Avizo® (see Appendix C). Overall, at low axial stress, the largest porosity reduction is observed in the Kfs sample, while the Qz sample is undergoing the smallest porosity change, roughly mirroring the stress-strain behaviour.

permanent strains. Note that only for the Kfs sample the strain achieved upon reloading appears to be apparent, i.e. within the measurement error. However, when comparing to the KfsQz and KfsQzC assemblies, which did show true additional compaction upon reloading, it is likely that also for the Kfs sample the strain resulting from reloading is true. Detailed micro-XCT images (see Appendix E) suggest that during reloading several grains have broken (Fig. E1a and -c), leading to rearrangement (Fig. E1b) of grains, while others show local crack growth (Fig. E1c). The former two can lead to small additional strains during reloading, while the latter suggests that reloading, and the concomitant slight additional compaction, may have increased the stresses at the crack tip, leading to crack propagation.

3.2. Microstructural data

3.2.1. Porosity evolution versus axial stress

The porosity evolution of the micro-XCT experiments is shown in Fig. 2b. It should be noted that samples Qz, Kfs and KfsQz show similar initial porosities, in the range of 39–42 %, whereas KfsQzC displays a significantly lower initial porosity of 32.9 ± 0.9 %. Overall, all experiments show comparable behaviour, in line with the observed mechanical behaviour (cf. Section 3.1). There is an initial, relatively rapid decrease in porosity with increasing stress (up to 20 MPa), followed by a more linear decrease in porosity, similar to what is seen for the stress-strain behaviour upon application of higher stresses (Fig. 2a). The Kfs sample undergoes more porosity reduction compared to the Qz sample (29.4 % vs. 17.9 %, respectively), despite these samples having very similar initial porosities. By contrast, the KfsQz and KfsQzC samples display comparable amounts of porosity reduction (21.9 % vs. 23.3 %, respectively), though sample KfsQzC has a much lower initial porosity. This is in accordance with the very similar stress-strain behaviour between the two Kfs-mixtures.

Unloading-reloading appears to lead to additional porosity reduction, similar to the observed increase in axial strain (detailed micro-XCT images are added in Appendix E). For the Qz, KfsQz and KfsQzC samples, this is observed as a roughly 1% increase in porosity during unloading, followed by 2 % porosity decrease during reloading. By contrast, the Kfs sample displays only 0.2 % porosity increase during unloading, and a 1 % porosity decrease during the subsequent reloading to 50 MPa. It should be noted that given the larger error in porosity, the observed porosity changes due to reloading are within the measurement error.

3.2.2. Grain size evolution

To compare grain size evolutions of the mm-sized, micro-XCT and cm-sized, conventional compaction experiments, all grain size distributions are expressed in terms of grain counting percentages (Fig. 3). This representation highlights the formation of numerous small particles, while such features are difficult to discern if the data would be plotted in terms of volume fractions (even large numbers of small grains still constitute only a relatively small volume). However, in interpreting Fig. 3, note that the total number of particles does not remain constant as grains break and chip. Consequently, the reductions seen in the counting fractions of larger grains will also include dilution-effects, as the total number of particles (grains and grain fragments) increases throughout the experiment. For the cm-sized Qz samples, an example comparison between the different possible data representations is provided in Appendix D.

From the Avizo®-based grain size evolution analyses, it can be observed that the grain size evolution of the micro-XCT Qz sand (Fig. 3a) shows a sharp, unimodal distribution at 150–250 μm , at the lowest axial stress (1.5 MPa; first scan). With increasing stress, the data shows a progressive decrease of the coarser fraction and the generation of particles with smaller grain sizes. Initially, only an increase of the 70–150 μm grain size fraction is observed. However, with increasing axial stress, a finer fraction of 20–40 μm is produced, which increases in proportion as deformation progresses. It should be noted that between the first 50 MPa load point and reloading to 50 MPa, there is a marked decrease of the 90–150 μm grain size fraction. At the end of the experiment, grains within the initial size range constitute about 50% of the grains in the aggregate. In the cm-scale Qz sand compaction experiments (Fig. 3b), the initial distribution of grain sizes (180–300 μm) also shows a strong reduction in proportion with increasing deformation, i.e. increasing axial stress. The decrease on the initial distribution is especially strong for the first loading steps, up to 30 MPa. Similar to the small-scale, micro-XCT experiments, the proportion of very fine particles (10–50 μm) grows with increasing deformation, but the cm-scale compaction tests show a larger proportion of fines. At the end of the experiment, the initial grain size fraction constitutes only 5% of the grains (Fig. 3b). However, note this does not represent breakage of 95% of the original grains, but rather reflects a marked increase in the total number of particles due to grain chipping and breakage (see Appendix D, Figure D2). For grain size analyses of samples retrieved from the cm-sized compaction experiments, approximately 50,000–60,000 particles

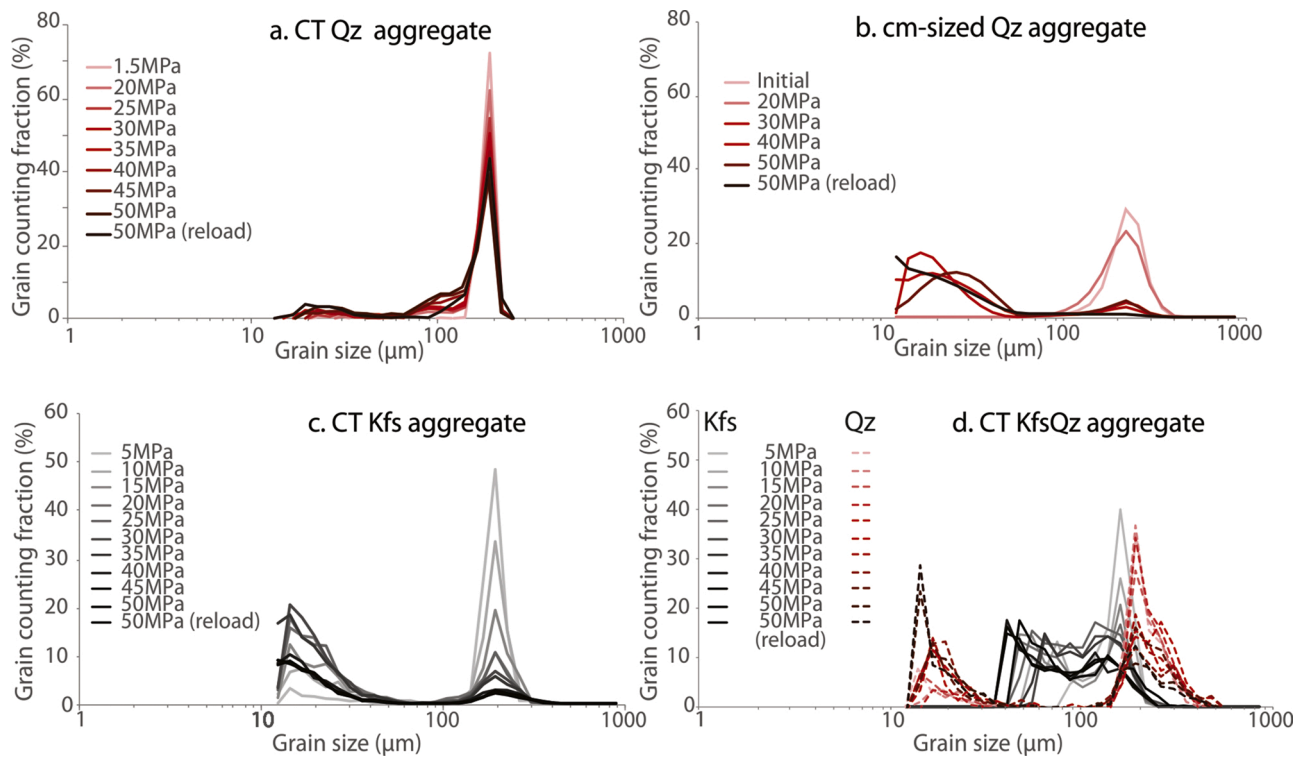


Fig. 3. Evolution of the grain size distribution for the a) micro-CT Qz experiment and b) cm-sized conventional oedometer-type experiments on Qz sand, as well as the micro-XCT experiments on the c) Kfs and d) KfsQz assemblies, all performed under dry, room-temperature conditions. Red lines show the grain size evolution of quartz particles, while grey lines represent K-feldspar grains. Note that the grain size distributions are cut off at $10\ \mu\text{m}$, due to the resolution of the micro-CT images. For the KfsQz sample, grains smaller than $\sim 30\ \mu\text{m}$ are erroneously identified as Qz only (d), while they most likely also include fine-grained Kfs (see Appendix B for further discussion).

are assessed. Conversely, for the micro-XCT images, only about 300 particles are accounted for, largely due to the much smaller sized samples.

For the pure Kfs sample (Fig. 3c), the initial grain size distribution is unimodal at the $150\text{--}250\ \mu\text{m}$ fraction. With increasing stress, there is a significant decrease in this fraction, due to the production of fines ($15\text{--}30\ \mu\text{m}$). By the end of the experiment, a bimodal distribution of grain sizes is observed, with a remarkable predominance of the finest fractions over the initial grain size (in the final stages, grains which roughly maintained their initial size constitute $<5\%$ of the sample). For the KfsQz mixture, the initial distributions of both Qz and Kfs grains are principally unimodal with most of the grains falling in the $150\text{--}300\ \mu\text{m}$ range (see Fig. 3d). With increasing stress, the two minerals evolve differently, with the Qz grains apparently generating significant amounts of fines ($15\text{--}35\ \mu\text{m}$). The Kfs grains also show significant grain size reduction, to a grain size fraction of $40\text{--}90\ \mu\text{m}$. It must be noted that it is possible that finer Kfs grains are present, but are wrongly identified as Qz grains due to an overlap in grey values (Appendix B). At the end of the experiment, the percentage of Qz grains keeping their initial grain size is larger than the percentage of Kfs grains doing so, though this may be partially due to increases in particle numbers.

3.3. Micro-X-ray computed tomography imaging: effect of mineralogy on microstructural evolution

Fig. 4 illustrates the full-scale configuration of the samples, taken at the centre of the aggregate at different axial stress values. This collection of images shows part of the PEEK vessel and the sample itself, which is composed by the grains of different mineralogies and the Teflon liner, i. e. the medium-grey, vertical to subvertical elements observed in the starting image. From the time-lapse micro-XCT images, it can be seen that, in the Qz sample, the first grain breakage occurs before or at 20

MPa applied stress, in localised portions of the sample, notably at its base where displacement is applied (Fig. 5a). As no scan was made between 1.5 and 20 MPa for this sample, the axial stress at which grain breakage initiates cannot be defined more precisely. Grain rearrangement likely played a significant role in the initial densification of the aggregate, resulting in a locked aggregate. For further compaction, grain breakage had to occur to unlock the aggregate. However, by the end of the experiment, a significant portion of the grains remains still unbroken, as also evidenced by the grain size analyses (cf. Section 3.2.2.) and detailed microstructural analysis (Fig. 6a).

For the Kfs sample, based on the analysis of the images, some of the grains have already clearly fractured at an axial stress of 10 MPa (Fig. 5b). However, the feldspar grains notably break along cleavage planes, as can be seen in Fig. 5b and 6b (see grain number 2 at 5 MPa axial stress). As axial stress is increased and deformation progresses, most of the Kfs grains break, resulting in a fined-grain fraction that occupies the pore space (Figs. 4b, 5c, 6b, and grain size distribution shown in Fig. 3c). Similarly, in the KfsQz assembly, the first K-feldspar grains start breaking at an axial stress of roughly 10 MPa (Fig. 7a), while the Qz grains only start showing grain failure at 20 MPa (Fig. 7b). By the end of the experiment, the majority of the Kfs grains are broken, partially filling the pore space with grain fragments, while many of the Qz grains remain intact (cf. Fig. 4c and 3d). This is also illustrated in Fig. 6c, where Qz grains 1, 2 and 4 remain unbroken, whereas the lighter grey Kfs grains, located above grain 3, are completely crushed.

As for the other Kfs-bearing sand, the Kfs grains in sample KfsQzC start breaking at a stress of ~ 10 MPa, but very locally and along cleavage planes (not shown). Based on the image analysis, some of the Qz grains start to break at 25 MPa, with cracks growing from one Qz-Qz contact to another (Fig. 7c). Only Qz grains which are in direct contact with other Qz grains tend to exhibit grain fracturing (Fig. 7b and c). The clay is too fine to identify any fracturing of the platelets, but it can be

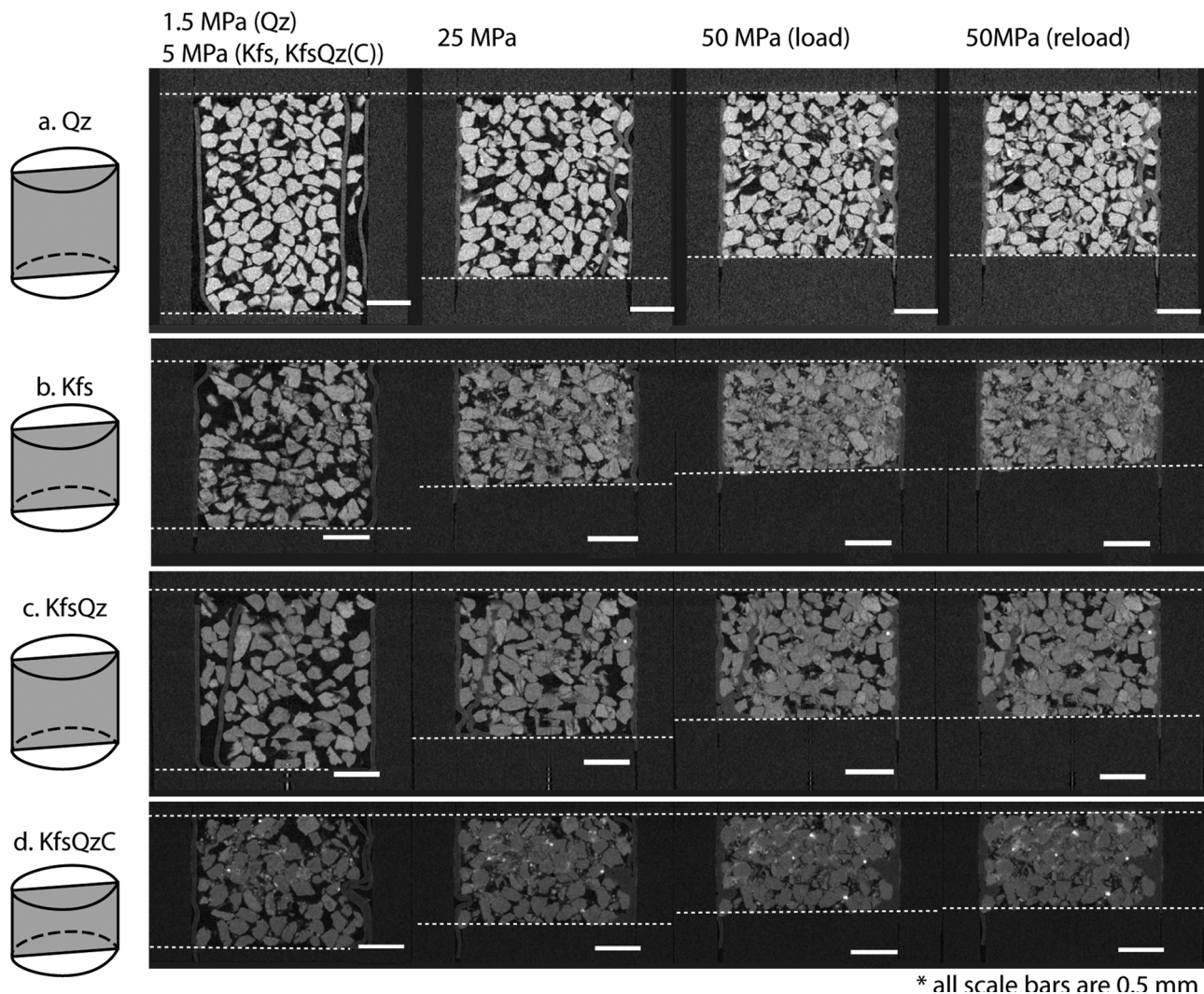


Fig. 4. Visual overview of the evolution of the aggregate microstructures at the start (at 1.5 MPa for Qz and 5 MPa for the other assemblies), at 25 MPa axial stress, at 50 MPa (load) and at the end of the experiment (50 MPa and reload to 50 MPa), for a) pure quartz, b) pure K-feldspar, c) KfsQz mixture and d) KfsQzC mixture. The dashed lines indicate the shortening of the sample in each stress step, compared to the fixed top of the sample. Note that the medium-grey vertical features are part of the Teflon liner placed inside the vessel.

seen that the clay tends to densify in response to compaction, by closing the pores in between the platelets and coagulation (seen by brighter grey values in Figs. 4d and 7d). At the maximum stress value, the pore space is largely occupied by the clays and the finer fraction resulting from Kfs breakage (Fig. 7d and 6d). However, only few Qz grains display fractures and some Kfs grains also remain intact (Fig. 6d).

4. Discussion

4.1. Effect of mineralogy on sand compaction behaviour

The mechanical and porosity evolution data obtained from the micro-XCT experiments indicate that the pure Qz sample has accumulated the least amount of strain at the maximum axial stress of 50 MPa, followed by KfsQzC, KfsQz and pure Kfs samples (Fig. 2a). Studies on sand aggregate compaction [9,25,66] have shown that the initial porosity, and hence also the grain coordination number, plays an important role in determining the stress-strain evolution, due to stress concentration at grain-to-grain contacts. However, the trends observed in these experiments appear to be largely controlled by the mineralogy of the sand aggregate, as initial porosities are similar for the Qz, Kfs and KfsQz samples (Table 1). Initial porosity values among the different

samples may vary by 3%, which would suggest a potential variation in volumetric (or axial) strain between the different samples of max. 3%, on the basis of these initial porosity variations. However, the variation in permanent strain is almost 12%, suggesting that factors other than porosity must also play a role. This fact is especially highlighted in the behaviour of the KfsQzC sample, which had the lowest initial porosity and accumulated the largest permanent strain (Fig. 2a and Table 1).

Instead, it is inferred that the difference in compaction behaviour is mainly controlled by the strength of the grains, which is directly related to the mineralogy. Typically, K-feldspar is considered a mechanically weak mineral [67–69], as it contains planes of weakness such as cleavage and twinning planes. This leads to the tendency of K-feldspar grains to fracture at lower applied stresses than the stronger quartz grains, as is observed in the microstructural analyses (Figs. 3–7). In addition to the grain strength, the Kfs grains are more angular than the Qz grains (Fig. 5), leading to enhanced stress concentrations at grain contacts and subsequent grain breakage at lower applied stresses [12]. However, a systematic investigation of grain morphology on compaction behaviour is outside the scope of our study. Once the grains have fractured, they do not tend to be crushed further (cf. Fig. 4b), likely because larger grains are shielded by the smaller grains, finer grains are generally stronger than larger ones (i.e. contain fewer structural flaws) and

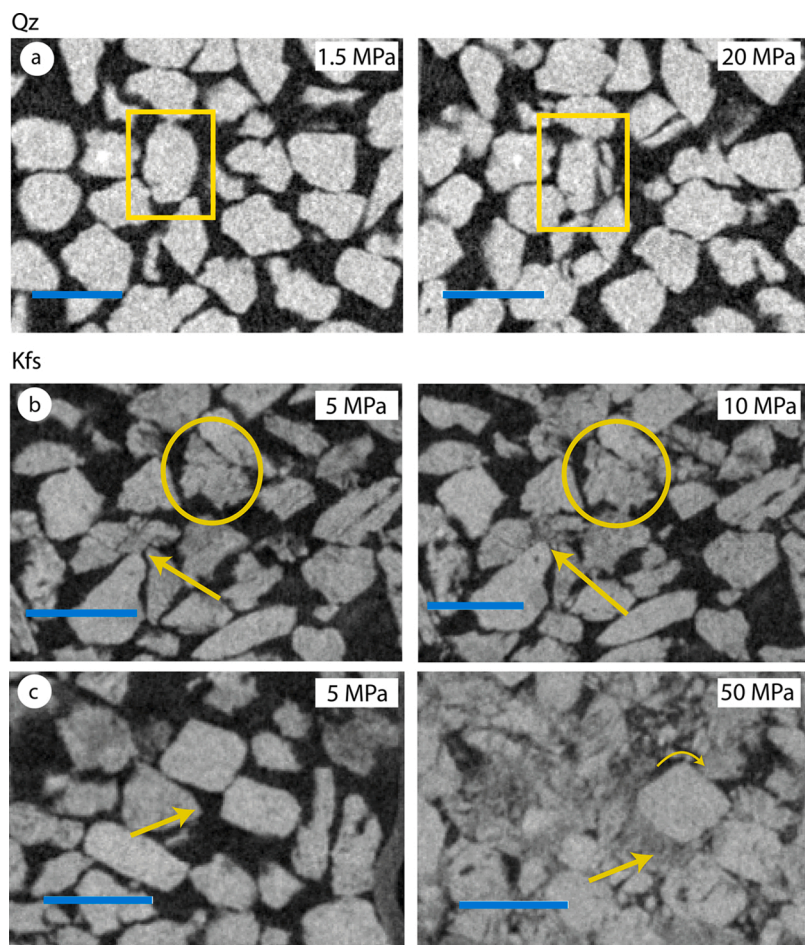


Fig. 5. Detailed micro-XCT images of the different mineral assemblies, illustrating the grain-scale processes that occurred during compaction (scale bar located at the bottom left: 300 μm). a) Qz grains start breaking at stresses below or up to 20 MPa. b) Kfs grains start breaking between 5 to 10 MPa as observed in the grain indicated with the arrow. The circle highlights also grain breakage, but in this case along cleavage planes. c) The arrow indicates the closure of the porosity and generation of a fine-grained fraction. Some of the grains rotate, as shown by the curved arrow on the 50 MPa-image.

porosity reduction leads to lower contact stresses [70,71]. Overall, fewer Kfs grains remain intact by the end of the experiment, compared to the pure Qz material, as also evidenced by the larger proportion of fines ($<50 \mu\text{m}$ – cf. Figs. 3a and c). In turn, this allows for more compaction and hence porosity reduction (cf. Figs. 4b, 5c and 6b) in Kfs-bearing material. Therefore, it is inferred that grain breakage, rearrangement and porosity reduction drive the progressive stiffening of the samples, with aggregate stiffness decreasing with increasing Kfs content (Fig. 2a).

For a mixed assembly of Qz and Kfs grains, the mechanical behaviour appears to be intermediate between the two end-members. It was previously described that compressibility increases with increasing feldspar content in unconsolidated sands [72], which also appears to be the case for the MARISCA device experiments. It should be noted that the grain size evolutions of Kfs in the KfsQz mixture suggest that the Kfs grains in this mixture break at lower stress values, but into larger fragments, compared to the grains in the monomineralic Kfs sample (see Fig. 3). Once the axial stress increases, the Qz grains also show grain size reduction, with significant production of fines, which could suggest chipping rather than whole grain failure. However, the micro-XCT images suggest that Kfs breaks into finer size fractions than observed in the grain size distribution determined using Avizo® (Figs. 4,5–7). It can be inferred that the limitations of the image processing do not allow accurate segmentation of Kfs and Qz for fine grain sizes (Appendix B). One can visually observe Kfs grains smaller than 30–40 μm in the images, but, due to partial volume effects, their grey values fall within the grey value range of quartz grains (Appendix B), leading to misidentifying them as Qz grains. The weak nature of the Kfs grains in Kfs-Qz contacts leads to breakage of the Kfs grains, and a reduction of the contact stress, before critical contact stresses can be built up in the Qz grains. Hence Qz grain failure is observed only at Qz-Qz contacts (see Fig. 7c).

For the KfsQzC sample, grain size distribution analysis was not possible due to limitations of the image processing related to overlapping grey values and partial volume effects associated with the presence of clays (Appendix B). The aggregate porosity loss is slightly larger for the KfsQzC than the KfsQz sample, though the initial porosity of the former is much lower than the latter ($32.9 \pm 0.9\%$ vs. $42.4 \pm 0.7\%$; Fig. 2b). Furthermore, upon visual inspection of the micro-XCT images, it does not appear that sample KfsQzC underwent significantly more grain fracturing. This suggests that the presence of clay in grain contacts facilitates the re-arrangement of grains by lowering intergranular friction, while clay in pores can be compacted further during loading [21]. Together this results in a porosity reduction similar to the KfsQz sample despite the lower initial porosity.

The unloading-reloading effect on the porosity (Fig. 2b) has been analysed in more detail and compared to the strain evolution (Fig. 2a). The apparent decrease in porosity of samples KfsQz and KfsQzC falls within the uncertainty associated with the calculation of the solid volume (see Appendix C). In the case of the Qz sample, the porosity reduction is associated with grain breakage and fracture propagation (see also Appendix E, where this is further corroborated using detailed images). Qz grain breakage occurs at stresses below 20 MPa, based on the grain size distributions (see Fig. 3a, b and Section 3.3). However, no micro-XCT measurements were made on the pure quartz samples at stresses below 20 MPa. From the grain size analysis of the KfsQz experiment, it appears that significant quartz grains fracturing occurred at an applied stress of >15 MPa. Based on the available observations, it can be inferred that for sand with an initial Qz and/or Kfs grain size of 150–250 μm , initial aggregate compaction at very low stresses likely occurs predominantly by grain rearrangement, until a locked aggregate is achieved [23]. By further increasing stress, grain breakage is observed

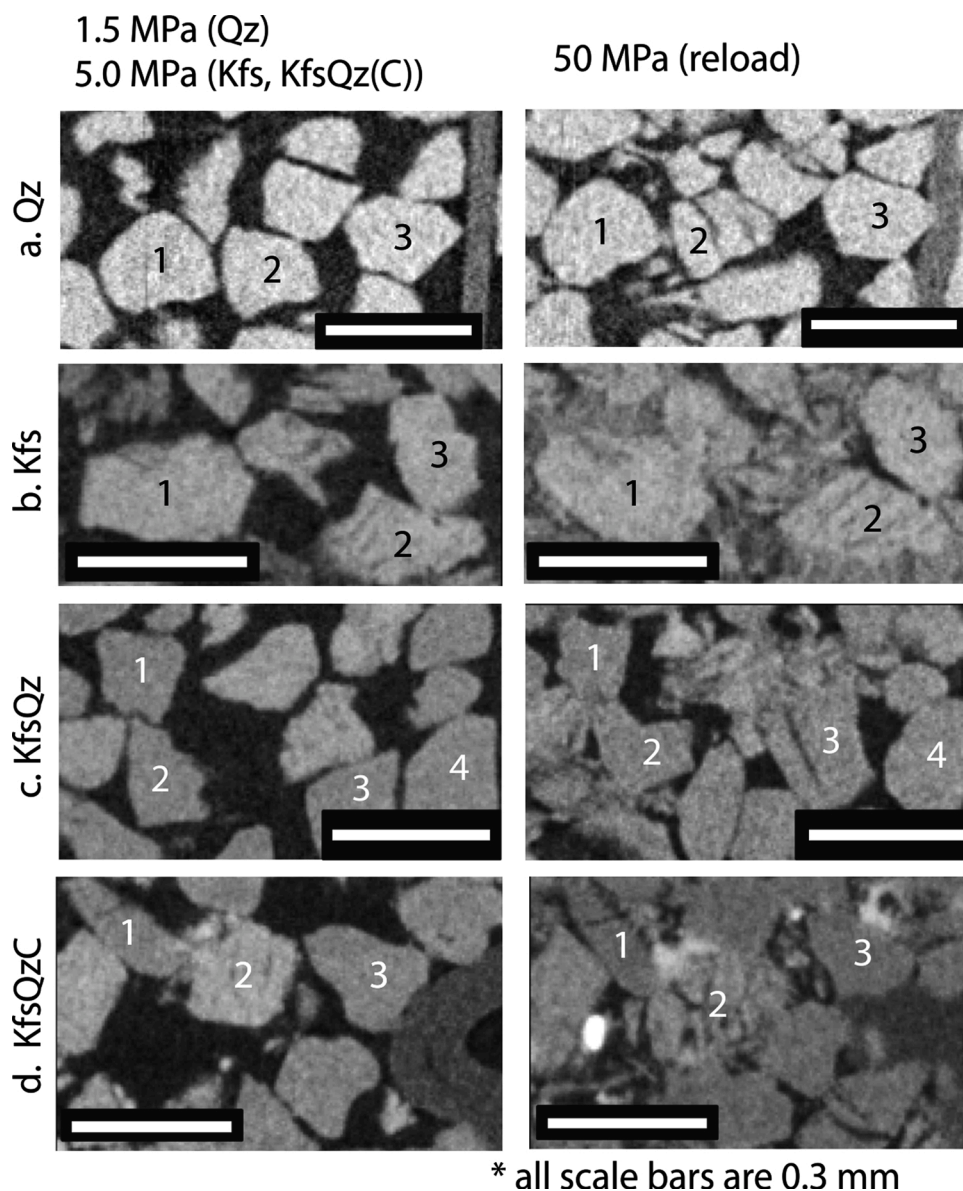


Fig. 6. Detailed micro-XCT images of the different mineral assemblies, illustrating the grain-scale processes that occurred during compaction of a) pure quartz, b) pure K-feldspar, c) KfsQz mixture, and d) KfsQzC mixture. The images in the left column show the distribution of the grains inside the vessel during the first scan (1.5 MPa for Qz and 5 MPa for the other assemblies). The images in the right column show the grain distribution at 50 MPa (reloaded). The numbers indicate grains that can be identified and tracked in both images; in c) only Qz grains are indicated with numbers, while in d) two Qz grains (1 and 3) and one Kfs grain (2) are shown. Note the tight packing and low porosity obtained in the Kfs and KfsQzC samples after deformation.

as the main mechanism leading to aggregate unlocking. With Kfs being the weaker mineral, in the Kfs-bearing mixtures the feldspar grains will show breakage along cleavage planes at axial stresses of 10 MPa or higher (Fig. 5b). As the feldspar grains become crushed, the grain size reduction and concomitant grain rearrangement will lead to further compaction, until the aggregate becomes locked again. Breakage of quartz grains occurs at higher axial stress values, though Qz grain failure will mainly propagate from Qz-Qz contacts (Figs. 7b and c).

With the addition of clays, there appears to be a delayed breakage of Qz grains, likely by preventing stress concentrations at grain contacts. Furthermore, any clay present in grain contacts reduces intergranular friction on these contacts [73], thereby facilitating grain sliding. As the aggregate becomes progressively denser, the clays, as well as grain fragments, fill the pore space.

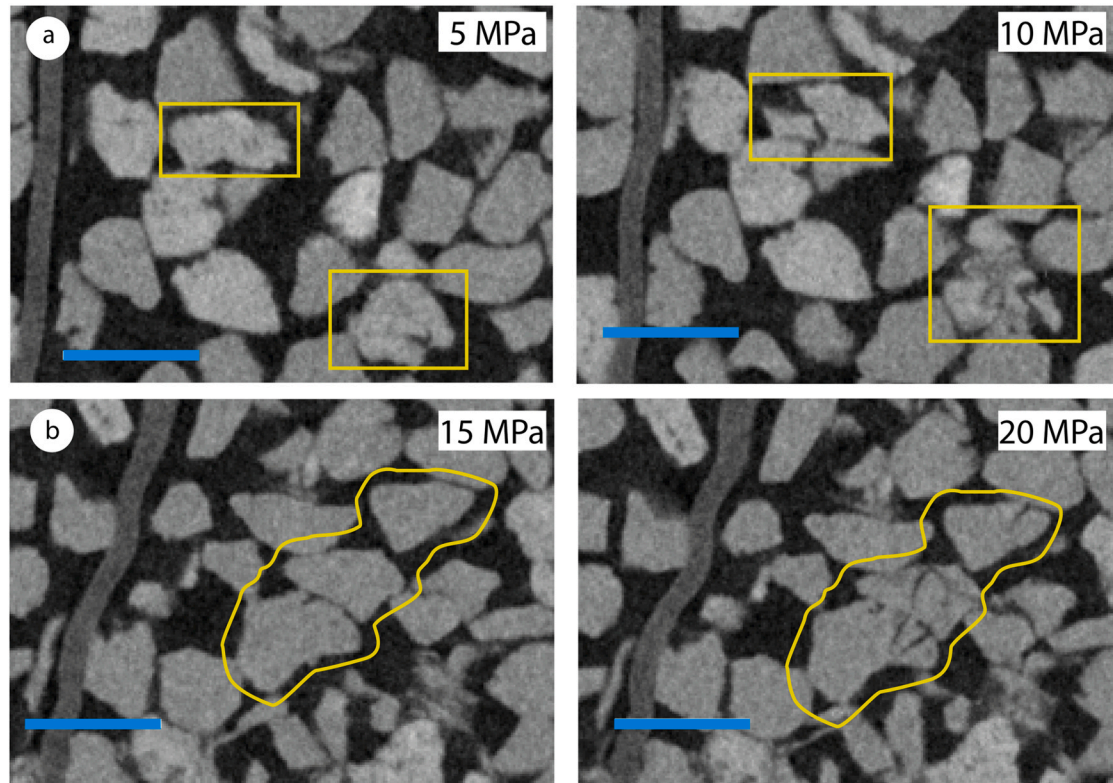
In summary, micro-XCT imaging has the potential to allow for the direct visualization of grain-scale processes that occur in compacting aggregates (i.e. grain sliding, crushing, grain-size evolution and porosity reduction).

4.2. Effect of sample dimensions on grain size evolution in the Qz experiments

While micro-XCT experiments provide valuable insight by allowing observation of grain scale processes, the method is limited to mm-sized samples to ensure the highest possible spatial resolution. This begs the question to what extent the microphysical processes observed in these relatively small volumes can be regarded as representative for larger-scale sand compaction behaviour. To explore for possible effects of sample size, a series of oedometer-type compaction experiments was performed on cm-scale Qz sand samples, allowing a comparison to be made in terms of how the grain size distributions evolve upon axial loading. Note such an analysis is necessarily qualitative, as comparative assessment of the oedometer and micro-XCT experiments will unavoidably suffer from uncertainties introduced by measurement limitations and differences in the two distinct analysis techniques used to obtain grain size distributions (Section 2.2.3, Appendix D).

Fig. 8a and b show the grain size evolution in the micro-XCT experiment and cm-scale reference tests, respectively. In order to facilitate a comparison, all data have been recalculated to numbers of grains per unit mass. Changes in the numbers of grains within the size fractions,

KfsQz



KfsQzC

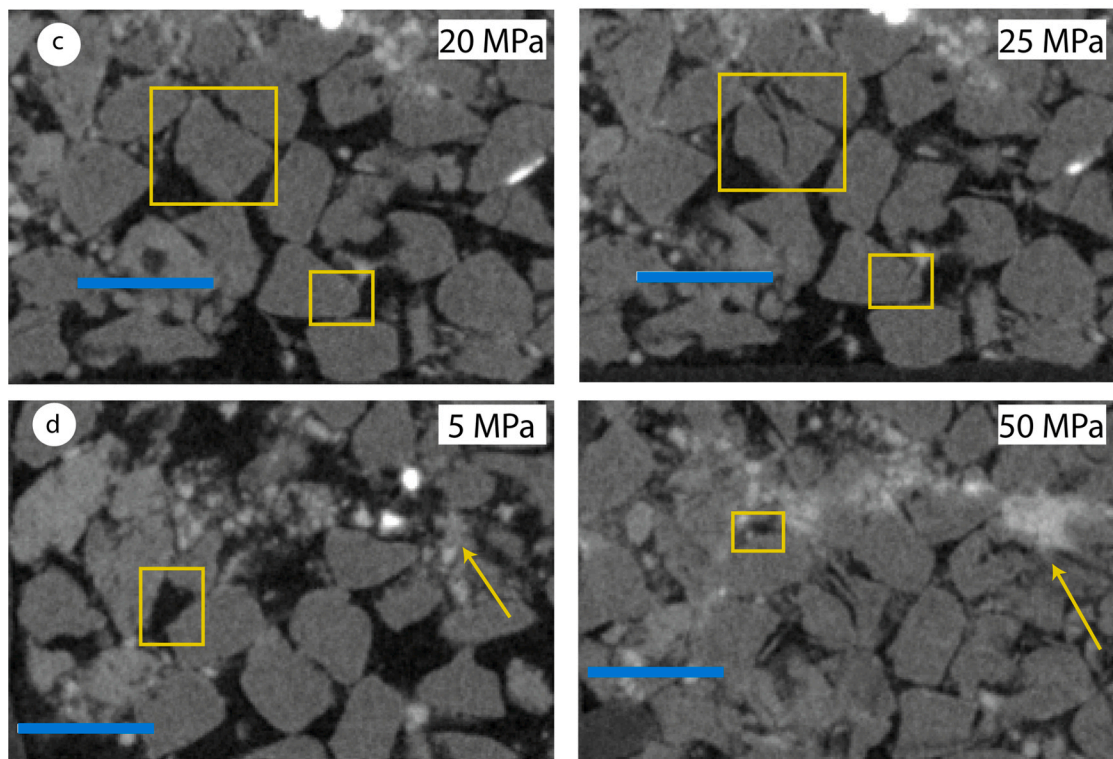


Fig. 7. Micro-XCT images of the mineral assemblies, illustrating grain-scale processes that occurred during compaction (scale bar: 300 μm). a) Kfs grains break between 5 and 10 MPa in the KfsQz sample as well. b) The Qz grains start breaking between 15 and 20 MPa, but only those ones in contact with other Qz grains. c) Qz grains break for the first time between 20 and 25 MPa in KfsQzC sample, but only when in contact with Qz grains. d) The pore space is filled with a fine-grained fraction for KfsQzC, as shown in the areas within the rectangles. The arrow highlights the densification of the clays due to the compaction and the consequential increase in grey values of the area.

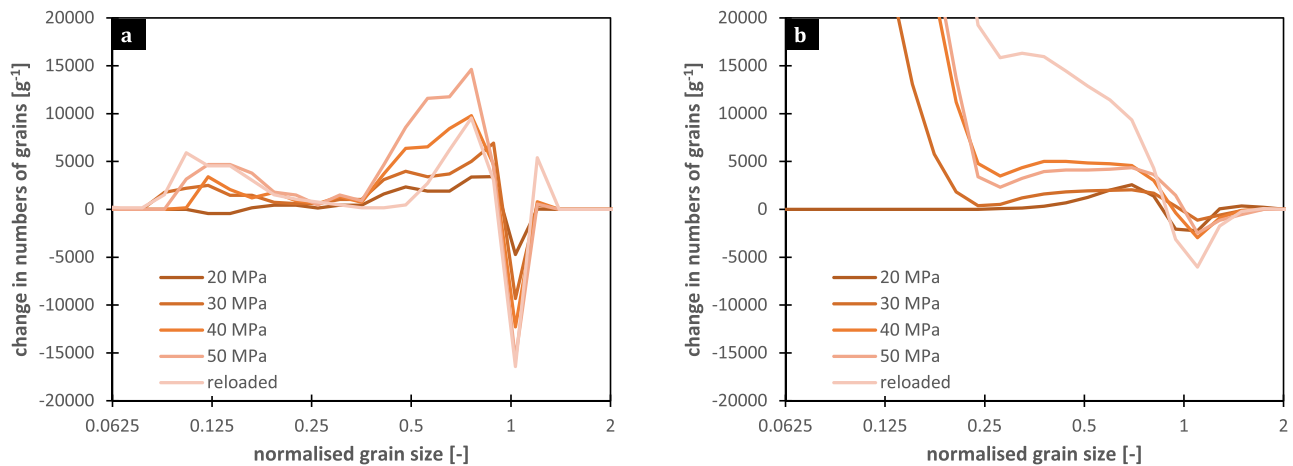


Fig. 8. Change in the numbers of grains per 1 g of Qz sample, relative to the initial sample grain size distribution, plotted as function of the grain size normalised with respect to the mean grain size of the initial sample material. Negative values show reductions in the numbers of grains, whereas positive values indicate the creation of additional particles (grains and fragments) in a specific size fraction. a) micro-XCT data for the mm-sized experiment performed in the MARISCA device, b) laser diffraction-based data for the series of cm-sized, reference compaction experiments (Section 2.3).

occurring upon sample loading, are obtained by subtracting the grain size distribution for the initial step (i.e. at 1.5 MPa) from the subsequent loading steps. Laser diffraction-based particle size analysis is known to overestimate the grain size compared to the sieved size fractions [10, 74], here yielding a measured mean grain size of 235 μm for the Qz material (Fig. 3b), which was sieved to $196 \pm 16 \mu\text{m}$. To facilitate the comparison, grain sizes plotted on the x-axes of Fig. 8 have therefore been normalised, i.e. divided by the mean grain size of the starting sample (at 1.5/5 MPa), using measured values of 185 and 235 μm for the micro-XCT and Malvern particle sizer-based data, respectively.

Comparing Fig. 8a and b, both the mm- and cm-sized samples show a reduction in the number of original grains (around $x = 1$), with a preference for grains slightly above the initial mean grain size ($x > 1$). It seems the micro-XCT experiment showed comparatively more breakage of grains (around $-15,000 \text{ g}^{-1}$ vs. -5000 g^{-1}), though it should be noted that the cm-sized samples have a broader initial grain size distribution (cf. Fig. 3a and b), which may impact the numbers of grains breaking within specific size bins. Both the micro-XCT and oedometer experiments further show the preferential formation of particles in two size domains, broadly around $x = 0.6$ and $x = 0.1$ (see e.g. 30 MPa curves, Fig. 8). Given these proportions of the original mean grain size, the two domains could perhaps represent “fragments” and “fines” resulting from breakage and chipping of Qz grains, respectively, phenomena that are also observed in the XCT images (see Appendix F for supporting images). Note that the cm-scale experiments show roughly similar amounts of fragments (on the order of $+5000$ to $+15,000 \text{ g}^{-1}$), but much more fines compared to the mm-sized sample. This difference could reflect resolution issues in the micro-XCT analysis (Section 2.2.4), or may be related to suspension and agitation of the cm-sized samples during laser diffraction-based particle size analysis [65], likely causing deagglomeration of damaged grains, which does not occur in the micro-XCT analysis.

The mm-sized sample of the micro-XCT experiment and cm-sized samples of the oedometer tests show qualitatively similar grain size evolution behaviour, with both forming particles of comparable proportions with respect to the mean grain size of the starting material. This provides some confidence that the mm-scale experiments display grain-scale processes that are also representative for sand compaction behaviour on larger scales. Nevertheless, it is possible that the larger reduction in the number of original-sized grains and the limited production of fines observed in the micro-XCT experiment could reflect differences in the amount of grain rearrangement allowed prior to the formation of a locked aggregate, e.g. due to wall-effects caused by the

sample container [75]. Additional research is required to obtain a better understanding of such scaling issues.

5. Conclusions

The influence of mineralogy on the compaction behaviour of unconsolidated sand aggregates is assessed through micro X-ray computed tomography (micro-XCT) imaging of uniaxial compaction experiments, performed at room temperature on dry, mm-sized samples. This technique allowed the microstructural processes operational at different stresses to be visualised at the grain-scale and under in-situ conditions. In total, four mineral assemblies have been investigated, namely pure quartz, pure K-feldspar, quartz + K-feldspar and quartz + K-feldspar + clay.

The micro-XCT experiments are complemented by conventional, oedometer-type compaction experiments, performed on cm-sized samples of the quartz sand, to consider possible effects due to sample size. Both aggregate sizes show qualitatively similar grain size evolutions during axial loading and compaction, with the initial formation of new particles occurring predominantly in two size domains, inferred to be associated with grain breakage versus chipping. The found similarities between the mm- and cm-sized experiments suggest the microphysical processes observed in the micro-XCT experiments are also, at least qualitatively, representative for larger-scale compaction behaviour.

From the micro-XCT experiments, it can be inferred that the difference in compaction behaviour between assemblies is mainly determined by mineralogy, as this controls grain strength. In the pure quartz and K-feldspar sands, it can be seen that quartz grain breakage occurs at stresses of <20 MPa, while feldspar breaks at lower stresses (<10 MPa), as the latter is a mechanically weak mineral due to its cleavage and twinning planes. Furthermore, the K-feldspar grains are more angular than the quartz grains, leading to higher contact stresses. After grain breakage, shielding effects and production of fines limit further breakage. Overall, fewer K-feldspar grains remain intact by the end of the experiment, compared to the quartz aggregates.

For the 80–20 vol% quartz-feldspar mixture, the mechanical behaviour is intermediate between the two end-members. Notably, the feldspar grains in such a mixture break at lower stresses, but into larger fragments, compared to the grains in the pure feldspar sample. At higher stresses, quartz shows grain chipping rather than whole grain breakage. It is inferred that the weak nature of the feldspar grains means that in quartz-feldspar contacts, stress build-up in the quartz grains is insufficient to induce quartz grain breakage. As a result, in this mixture, quartz

grain breakage mainly occurs at quartz-quartz contacts.

In the presence of clays, in grain contacts and pores, grain rearrangement is facilitated by a lowering of intergranular friction, while clay in pores can be compacted further during loading. Quartz breakage occurs at higher stresses than in clay-free aggregates, likely due to clay compaction preventing grain contact stress concentrations.

Overall, it is inferred that grain breakage, rearrangement and porosity reduction drive the progressive stiffening of the sand samples, with aggregate stiffness decreasing with increasing K-feldspar content. The experiments have shown that micro-XCT imaging has the potential to allow for direct visualization of grain-scale processes that occur in compacting aggregates.

Funding

This study was carried out in the context of the research program funded by the Nederlandse Aardolie Maatschappij (NAM). This program aims to fundamentally improve understanding of production-induced reservoir compaction and seismicity in the seismogenic Groningen gas field. We thank the team at NAM for permission to publish this study. J. V.F.S. was supported by this project, he is currently an FWO post-doctoral researcher and acknowledges the support through project 12ZV820 N. T.K.T.W. was supported under grant PT63253. For the Deben CT5000 apparatus, the Research Foundation Flanders (FWO) is acknowledged under project G.0041.15 N. FCWO-UGent is also acknowledged for their support for purchasing this device.

Data availability

All micro-XCT images, as well as the All micro-XCT images, as well as the data on the grain size distribution and the mechanical data used for this paper are available through <https://doi.org/10.24416/UU01-DHYKQ1>, on the Yoda data publication platform of Utrecht University.

Declaration of Competing Interest

The authors declare that they have no known competing financial interests or personal relationships that could have appeared to influence the work reported in this paper.

Acknowledgments

The Centre for X-ray Tomography at Ghent University (UGCT) is acknowledged for the use of their facilities. M. Deprez is thanked for his help in reconstructing part of the datasets. F. van Oort and A. van der Gon-Netscher are acknowledged for designing and building the add-on for the CT5000 apparatus to construct the MARISCA device. We thank the editor, Alexander Lunt, and two anonymous reviewers for their detailed feedback, which benefitted the manuscript.

Appendices A–F. Supplementary data

Supplementary material related to this article can be found, in the online version, at doi:<https://doi.org/10.1016/j.mtcomm.2020.101881>.

References

- R.M. Ostermeier, SPE Form. Eval. 10 (1995) 79–85.
- R.P.J. Pijnenburg, B.A. Verberne, S.J.T. Hangx, C.J. Spiers, J. Geophys. Res. Solid Earth 123 (2018) 5532–5558.
- C.J. Spiers, S.J.T. Hangx, A.R. Niemeijer, Geol. En Mijnbouw/Netherlands J. Geosci. 96 (5) (2017) s55–s69.
- J. Suckale, Lead. Edge (Tulsa, OK) (2010) 310–319.
- C. Haug, J.A. Nüchter, A. Henk, Geomech. Energy Environ. 16 (2018) 15–31.
- S. Xu, F. Hao, C. Xu, Y. Wang, H. Zou, C. Gong, Mar. Pet. Geol. 63 (2015) 1–16.
- R.M. Bernabé, Y. Fryer, D.T. Shively, Geophys. J. Int. 117 (1994) 403–418.
- E. Shalev, V. Lyakhovskiy, A. Ougier-Simonin, Y. Hamiel, W. Zhu, Geophys. J. Int. 197 (2014) 920–925.
- R.H. Brzesowsky, C.J. Spiers, C.J. Peach, S.J.T. Hangx, J. Geophys. Res. Solid Earth 119 (2014) 936–956.
- S.J.T. Hangx, N. Brantut, J. Geophys. Res. Solid Earth 124 (2019) 6560–6580.
- M.T.W. Schimmel, S.J.T. Hangx, C.J. Spiers, J. Geophys. Res. Solid Earth 124 (2019) 5584–5606.
- R. Alikarami, A. Torabi, Geomech. Energy Environ. 3 (2015) 1–10.
- F.M. Chester, J.S. Chester, A.K. Kronenberg, A. Hajash, J. Geophys. Res. Solid Earth 112 (2007), B06203.
- S.L. Karner, J.S. Chester, F.M. Chester, A.K. Kronenberg, A. Hajash, Am. Assoc. Pet. Geol. Bull. 89 (2005) 603–625.
- A. Tengattini, A. Das, I. Einav, Gotechnique 66 (2016) 695–710.
- A. Tengattini, A. Das, G.D. Nguyen, G. Viggiani, S.A. Hall, I. Einav, J. Mech. Phys. Solids 70 (2014) 281–296.
- Y. Bernabé, D.T. Fryer, J.A. Hayes, Geophys. Res. Lett. 19 (14) (1992) 1511–1514.
- F. Saidi, Y. Bernabé, T. Reuschlé, Tectonophysics 370 (2003) 105–120.
- H. Yin, J. Dvorkin 21 (1994) 903–906.
- F.A. Chuhan, A. Kjeldstad, K. Bjørlykke, K. Høeg, Mar. Pet. Geol. 19 (2002) 39–53.
- F.A. Chuhan, A. Kjeldstad, K. Bjørlykke, K. Høeg, Can. Geotech. J. 40 (2003) 995–1011.
- R.H. Brzesowsky, S.J.T. Hangx, N. Brantut, C.J. Spiers, J. Geophys. Res. Solid Earth (2014) 7521–7541.
- G. Mesri, B. Vardhanabhuti, Can. Geotech. J. 46 (2009) 369–392.
- T.W. Lambe, R.V. Whitman, Soil Mechanics, John Wiley, New York, 1969.
- I. Borg, M. Friedman, J. Handin, D.V. Higgs, Mem. Geol. Soc. Am. (1960) 133–191.
- S.J.T. Hangx, C.J. Spiers, C.J. Peach, J. Geophys. Res. Solid Earth 115 (2010).
- J. Fortin, S. Stanchits, G. Dresen, Y. Guéguen, J. Geophys. Res. Solid Earth 111 (2006), B10203.
- P. Baud, E. Klein, T. fong Wong, J. Struct. Geol. 26 (4) (2004) 603–624.
- R.P.J. Pijnenburg, B.A. Verberne, S.J.T. Hangx, C.J. Spiers, J. Geophys. Res. Solid Earth (2019).
- V. Cnudde, M.N. Boone, Earth-Sci. Rev. 123 (2013) 1–17.
- R. Alikarami, E. Andò, M. Gkiouas-Kapnis, A. Torabi, G. Viggiani, Acta Geotech. 10 (2015) 15–30.
- E. Andò, S.A. Hall, G. Viggiani, J. Desrues, P. Bésuelle, Acta Geotech. (2012).
- Z. Karatza, E. Andò, S.A. Papanicolopoulos, G. Viggiani, J.Y. Ooi, Granul. Matter (2019).
- B. Zhao, J. Wang, E. Andò, G. Viggiani, M.R. Coop, Can. Geotech. J. (2020).
- M.F. Alam, A. Haque, P.G. Ranjith, Materials (Basel) (2018).
- G. Guida, F. Casini, G.M.B. Viggiani, E. Andò, G. Viggiani, Geotech. Lett. (2018).
- E. Salvatore, E. Andò, G. Viggiani, G. Modoni, 1st IMEKO TC4 Int. Work. Metrolog. Geotech. Metrogeotechnics 2016, 2016.
- E. Salvatore, E. Andò, G. Modoni, G. Viggiani, Procedia Eng. (2016).
- E. Andò, G. Viggiani, S.A. Hall, J. Desrues, Géotechnique Lett. 3 (2013) 142–146.
- L. Zhang, M. Pan, H. Wang, Acta Geol. Sin. (2017) 283–300.
- R.A. Davis, Habitats Biota Gulf Mex. Before Deep. Horiz. Oil Spill, 2017, pp. 165–215.
- K.W. Glennie, in: J. Grötsch, R. Gaupp (Eds.), The Permian Rotliegend of The Netherlands, SEPM Special Publication, Tulsa, Oklahoma, USA, 2011.
- J. De Jager, C. Visser, Geol. En Mijnbouw/Netherlands J. Geosci. 96 (2017) s3–s15.
- W.E. Westerhoff, (n.d.).
- D. Borden, R.F. Giese, Clays Clay Miner. 49 (5) (2001) 444–445.
- A. Nadeev, D. Mikhailov, E. Chuvilin, D. Koroteev, V. Shako, Microsc. Anal. (Am. Ed.) 27 (2013) 8–10.
- A. De Muynck, S. Bonte, J. Dhaene, M. Dierick, K. Bacher, L. Van Hoorebeke, M. N. Boone, Nucl. Instrum. Methods Phys. Res. Sect. B Beam Interact. Mater. Atoms (2019).
- J. Dhaene, E. Pauwels, T. De Schryver, A. De Muynck, M. Dierick, L. Van Hoorebeke, Nucl. Instruments Methods Phys. Res. Sect. B Beam Interact. Mater. Atoms (2015).
- R. Gaupp, A. Matter, J. Platt, K. Ramseyer, J. Walzebuck, Am. Assoc. Pet. Geol. Bull. (1993).
- S. Waldmann, R. Gaupp, Sediment. Geol. (2016).
- M.D. Wilson, Orig. Diagenesis Petrophysics Clay Miner. Sandstones (1992).
- J.F. Van Stappen, T. De Kock, G. De Schutter, V. Cnudde, Bull. Eng. Geol. Environ. 78 (2019) 5301–5310.
- J.H. Schön, Dev. Pet. Sci. 65 (2015) 269–300.
- E. Fjaer, R.M. Holt, P. Horsrud, A.M. Raaen, R. Risnes, Pet. Relat. Rock Mech. (1992).
- J.W. Dudley, M. Brignoli, B.R. Crawford, R.T. Ewy, D.K. Love, J.D. McLennan, G. G. Ramos, J.L. Shafer, M.H. Sharf-Aldin, E. Siebrits, J. Boyer, M.A. Chertov, Rock Mech. Rock Eng. (2016).
- M. Dierick, D. Van Loo, B. Masschaele, J. Van Den Bulcke, J. Van Acker, V. Cnudde, L. Van Hoorebeke, Nucl. Instrum. Methods Phys. Res. Sect. B Beam Interact. Mater. Atoms 324 (2014) 35–40.
- B.C. Masschaele, V. Cnudde, M. Dierick, P. Jacobs, L. Van Hoorebeke, J. Vlassenbroeck, Nucl. Instruments Methods Phys. Res. Sect. A Accel. Spectrometers, Detect. Assoc. Equip. 580 (2007) 266–269.
- J. Vlassenbroeck, M. Dierick, B. Masschaele, V. Cnudde, L. Van Hoorebeke, P. Jacobs, Nucl. Instrum. Methods Phys. Res. Sect. A Accel. Spectrometers, Detect. Assoc. Equip. 580 (2007) 442–445.
- J. Schindelin, I. Arganda-Carreras, E. Frise, V. Kaynig, M. Longair, T. Pietzsch, S. Preibisch, C. Rueden, S. Saalfeld, B. Schmid, J.Y. Tinevez, D.J. White, V. Hartenstein, K. Elceiri, P. Tomancak, A. Cardona, Nat. Methods 9 (7) (2012) 676–682.

- [60] (n.d.).
- [61] C. Jaquet, E. Andó, G. Viggiani, H. Talbot, *Int. Symp. Math. Morphol.* (2013) 452–463.
- [62] M. Zhang, S.M. de Jong, C.J. Spiers, A. Busch, H.M. Wentinck, *Int. J. Greenh. Gas Control* 74 (2018) 49–61.
- [63] R. van Noort, T.K.T. Wolterbeek, M.R. Drury, M.T. Kandianis, C.J. Spiers, *Minerals* 7 (2017) 1–31.
- [64] E. Liteanu, C.J. Spiers, *Chem. Geol.* 265 (2009) 134–147.
- [65] Malvern Instruments, *S. Mastersizer, Getting Started MAN0101*, 1997.
- [66] R. Brzesowsky, *Micromechanics of Sand Grain Failure and Sand Compaction*, Utrecht University, 1995.
- [67] S. Morad, in: G.V. Middleton, M.J. Church, M. Coniglio, L.A. Hardie, F.J. Longstaffe (Eds.), *Encycl. Sediments Sediment. Rocks*, Springer Netherlands, Dordrecht, 2003, pp. 278–281.
- [68] Marloes Jongerius, *Reservoir Compaction in Shallow Gas Reservoirs: the Impact of Production-induced Reservoir Compaction on the Recovery of Gas From Shallow Reservoirs*, Technische Universiteit Delft, 2016.
- [69] S. Hol, A. Van Der Linden, S. Bierman, F. Marcelis, A. Makurat, *Sci. Rep.* 8 (2018) 1–13.
- [70] N.J. Petch, *J. Iron Steel Inst.* 174 (1) (1953) 25–28.
- [71] C. Sammis, G. King, R. Biegel, *Pure Appl. Geophys. PAGEOPH* 125 (5) (1987) 777–812.
- [72] C.T. Sawabini, G.V. Chilingar, D.R. Allen, *Soc. Pet. Eng. AIME J.* 14 (2) (1974) 132–138.
- [73] S. Tembe, D.A. Lockner, T.F. Wong, *J. Geophys. Res. Solid Earth* 115 (2010), B03416.
- [74] A.M.H. Pluymakers, C.J. Peach, C.J. Spiers, *J. Geophys. Res. Solid Earth* 119 (2014) 4123–4148.
- [75] D.E. Karig, G. Hou, *J. Geophys. Res. Solid Earth* 97 (1992) 289–300.